Selection of cathode materials for forsterite supported solid oxide fuel cells – Part 1: Materials Interactions

Authors: Fabian Grimm[a*], Norbert H. Menzler[a], Olivier Guillon [a,b]

[a] Forschungszentrum Jülich GmbH, Institute of Energy and Climate Research, Materials Synthesis and Processing (IEK-1), 52425 Jülich, Germany

[b] JARA-ENERGY, 52425 Jülich, Germany

*f.grimm@fz-juelich.de

Keywords:

- Solid oxide fuel cell
- Interactions
- Forsterite
- Cathode
- Performance

Abstract:

An inert-supported cell (ISC) was developed by Bosch with the aim of lowering the manufacturing costs of SOFCs and thus increasing their marketability and prolonging their lifetime. This ISC concept uses forsterite, a manganese silicate doped with Zn and Ca, as support material. The cell can be described as air side inert-supported cell, since forsterite faces the air compartment.

Forsterite was chosen as a support material, as it is abundant and therefore relatively inexpensive. All functional layers are subsequently applied and co-sintered at T<1300 °C to further reduce cell manufacturing costs.

At present, LSM is used as a cathode. However, the performance of the cell is drastically reduced due to the formation of a Zn–Mn spinel at the triple-phase boundaries during co-firing.

Based on these findings, seven different cathodes were synthesized to identify a cathode that is less reactive with forsterite. In order to investigate their reactivity, different types of samples were prepared: mixed pellets, double-layered pellets and screen-printed cathode inks on forsterite green substrates. These samples and their cross sections were then investigated by using XRD, SEM, EDX, and WDX. Their reactivity was as follows (ascending order): LSFM > LSF > LSC > PSCF > LSCF > LCCF

1 Introduction

Solid oxide fuel cells (SOFCs) are highly efficient, low-emission, flexible-fuel conversion devices that play a crucial role in reducing greenhouse gases for a future renewable energy environment. [1] A huge variety of different fuel cell types have been developed over the last 20–30 years. [1-6] SOFCs can be subdivided into four major cell types: electrode, electrolyte, metal and inert-supported cells. Each cell type has its own advantages and disadvantages. [4] In general, a low-cost SOFC is targeted in order to increase its marketability. The number of manufacturing steps required (e.g. shaping, casting, coating, cutting, handling, etc.), the sintering conditions and the costs of each layer therefore play a crucial role in the costs of the different cell types. [7]

The anode-supported cell (ASC) gains its mechanical stability from a relatively thick, porous anode layer (> 200µm). This porous tape cast support enables a high fuel gas feed charge. A thin (5-10µm), fine-graded functional layer consisting of NiO and 8YSZ is tape cast or screen printed on top of the porous support in order to increase the number of triple-phase boundaries. As the mechanical stability of the cell is based on the anode support layer, the electrolyte thickness is rather low at 2–20µm. This enables low ohmic resistances and low operating temperatures. [8] However, after each manufacturing step, a separate sintering step is typically required. After applying the diffusion barrier layer (if high performance cathodes are used), the cathode, and the current collector, the total number of sintering steps amounts to three up to five, depending on the chosen materials. [9] This number of heat treatment steps can be further reduced by using, for example, the promising method of multilayer sequential tape casting as described by Menzler et al.[7].

Similar to the multi-sequential tape cast ASC, the electrolyte-supported cells (ESCs) can also be realized in just two heat treatment steps. The ESC manufacturing route starts with the tape casting of the electrolyte followed by cutting in the desired shape and a first sintering step. The electrolyte is then screen-printed with the electrodes and finalized in a second heat treatment step. [10] With a relatively thick electrolyte of ≥100µm, the electrolyte-supported cell gains its mechanical stability from the electrolyte layer. An advantage of the ESC design is its very low leakage rate, although the desired ionic conductivity for such a thick electrolyte requires relatively high operating temperatures of ~900 °C due to the high ohmic resistance. [8]

Another method of reducing material and manufacturing costs is the utilization of a porous metal support. The metal-supported cell (MSC) takes advantage of cheap metals (cheap compared to ceramic supports based on e.g. YSZ and/or Ni), mostly containing Fe and Cr, meaning that thick – and therefore expensive – anode or electrolyte layers are not required. [11] The operating temperatures of MSCs are typically rather low (≈ 600°C e.g. Ceres Power [12]). However, using metal as a support poses new challenges, as the sintering of the cell must be performed in a reducing atmosphere or vacuum so that no corrosion takes place. Furthermore, interdiffusion between the metal support and the anodic nickel plays a crucial role, while oxide scale formation at high water vapor pressures might be detrimental. [13, 14]

Comparison of these different cell designs with respect to the scaling up of a low-cost cell serves to underline the crucial factor: Material prices. [15] Therefore, alternative materials that are cost-efficient, abundant and fulfill the respective requirements are also desired.

Upon closer inspection of the ASC, ESC, and MSC cell designs, it becomes clear that a cost-effective support material (the thickest layer in the cell), a thin electrolyte (to lower the ohmic losses and the operating temperatures), and the absence of metal to avoid cost intensive vacuum sintering steps are all part of the requirements of a low-cost SOFC. [16] With these aspects in mind, the inert-supported cell (ISC) potentially fulfils all of these criteria. It utilizes cheap porous materials as a support, which can either be applied at the fuel [17] or air side. [18] This concept has been used in the past, for instance by Rolls-Royce [17] and TOTO [19].

Within a public funded project an ISC concept based on forsterite, an abundant and cheap manganese silicate, as support material on the air side was developed. [18] To enhance the marketability of this ISC concept, a reasonable approach would be to further reduce the number of sintering steps by co-firing all the layers in just one heat treatment step.

However, during co-firing, the different layers might form undesired reaction phases with the support material forsterite. Furthermore, co-firing has an impact on the microstructure and porosity of each layer. These changes can have a huge impact on the output power density of the SOFC. [18] Therefore, one of the focal points of the present work is the selection of a cathode material that exhibits low tendency to react with forsterite and which does not lose its catalytic activity.

To our knowledge, forsterite has not yet been used for SOFCs. In the literature, most publications concerning forsterite focus on the synthesis and the effect of different dopants on the mechanical and electrical properties. This is because forsterite is mostly used for medical purposes and for radar systems. Forsterite is a material belonging to the mineral group olivine with superior electrical and thermal insulating properties. [20, 21] Its basic oxides are abundant, making forsterite (Mg_2SiO_4) a low-cost material. [22]

The first synthesis methods for forsterite were developed in the mid-20th century. Different groups reported the synthesis of an olivine single crystal (forsterite) using the Czochralski process. This is a costly process due to the melting of the educts MgO and SiO_2, which requires high temperatures ($T>1800\,°C$). [22-24] To avoid high temperatures, various synthesis approaches such as the solid-state reaction or the sol–gel synthesis can be found in the literature. For the solid-state reaction, Nurbaiti et al. [25] reported the synthesis of forsterite based on MgO and SiO_2 at 1200 °C. Tavangarian and Emadi [26] lowered the synthesis temperature to 1000 °C using talc, magnesium carbonate, and ammonium chloride as educts. Other groups [20, 27-30] reported the sol–gel synthesis of Mg_2SiO_4 or forsterite-like compositions at $T<1100\,°C$ using different educts.

Within the R&D project forsterite doped with Zn and Ca which is in contact with LSM as cathode material is used. To date, the performance of the cell is rather low due to Zn–Mn spinel formation at the triple-phase boundaries and the impact of co-firing on the microstructure. [18, 31]

The aim of this study is to identify a cathode material exhibiting either no or limited reaction and interdiffusion with forsterite or which interaction phases do not influence the cell performance too much. To do so, different cathode materials were screen printed on forsterite, heat-treated at <1300°C, and analyzed in terms of their interdiffusion and crystallographic interactions. In the second part of the paper, the cathodes are electrochemically characterized using impedance spectroscopy.

2 Experimental

Forsterite (Mg_2SiO_4) doped with Zn and Ca, provided by Bosch was used as substrate material as a green plate with the dimensions 29·x 29·x 1.5mm³ as well as powder with a d_{50} of 2.58µm. Seven different cathode materials were screen printed with a wet layer thickness of 272µm on the forsterite green plate. Each cathode material (62.75 wt%) was mixed with 20,85 wt% terpineol (DuPont) and 16.4 wt% of a transport medium consisting of 6 wt% of 45 cp ethyl cellulose and terpineol. The chosen cathode materials were LSCF ($La_{0.58}Sr_{0.4}Co_{0.2}Fe_{0.8}O_3$), LSC ($La_{0.58}Sr_{0.4}CoO_3$), LSF ($La_{0.58}Sr_{0.4}FeO_3$), PSCF ($Pr_{0.58}Sr_{0.4}Co_{0.2}Fe_{0.8}O_3$), LCCF ($La_{0.58}Ca_{0.4}Co_{0.2}Fe_{0.8}O_3$), LSFM 95S1M3 ($(La_{0.9}Sr_{0.1})_{0.95}Fe_{0.7}Mn_{0.3}O_3$), and LSFM 95S2M8 ($(La_{0.8}Sr_{0.2})_{0.95}Fe_{0.2}Mn_{0.8}O_3$).

LSCF is the current state-of-the-art cathode for SOFCs and has a high performance when thin-film electrolytes are used. [8, 32-35] LSC and LSF were selected to characterize the effect of the respective B-site perovskite elements, (Co and Fe respectively) on the reactivity with forsterite. Furthermore, compared to LSCF, LSC is known to be even more electrocatalytically active [32]. With LSF, electrocatalytic activity is inferior to LSCF, although LSF exhibits better temperature stability [32]. With PSCF and LCCF, the influence of a different A-site element can be visualized and analyzed, as this is the only difference between these two cathode materials in comparison to the state-of-the-art LSCF. For LCCF, the influence of excluding Sr can be analyzed, while PSCF demonstrates the impact of the absence of La. Furthermore, LCCF should exhibit more stable behavior compared to LSCF, as Co has an atomic radius which only slightly differs from that of La (Co=1.34 Å; La=1.36 Å and Sr=1.44 Å [36]). The atomic radii mismatch in relation to that of La is therefore kept to a minimum for Ca compared to Sr. [37]

In order to exclude possible influences of different compositions, the overall stoichiometric composition of the respective perovskites $(A_{0.58}A'_{0.4})B_{0.2}B'_{0.8}O_3$ were kept constant. A base composition with A-site sub-stoichiometries was chosen, as this stoichiometry represents the current state-of-the-art LSCF composition. [35] The two LSFM compositions were chosen to demonstrate the influence of low and high Mn concentrations at the B-site in comparison to the currently used LSM. Furthermore, it is known that the two LSFM compositions do not react with 8YSZ [38], the state-of-the-art electrolyte which is used for SOFCs and might exhibit better long-term stability, since Mn is identified as playing a crucial role in terms of long-term stack stability. [39] LSCF, LSC, LSF and PSCF were synthesized in-house via spray pyrolysis route where stoichiometric amounts of the respective nitrates were added to the combustion chamber for the reaction. [40, 41] LSFM 95S1M3, LSFM 95S2M8, and LCCF were synthesized using the Pechini method. For both LSFM compositions, stoichiometric amounts of lanthanum nitrate hexahydrate [$La(NO_3)_3 \cdot 6H_2O$; 99,99 %; Alfa Aesar], strontium nitrate hexahydrate [N_2O_6Sr; 99 %; Sigma-Aldrich], iron nitrate nonahydrate [Alfa Aesar; 98-101 %; $Fe(NO_3)_3 \cdot 9H_2O$], and manganese nitrate tetrahydrate [$Mn(NO_3)_2 \cdot 4H_2O$; ≥98.5 %; Emsure] were completely dissolved in water. An excess amount of 20 % citric acid was added to the solution as a complexing agent. After 1h of stirring, ethylene glycol was added as a chelating agent. This was followed by controlled heating up to 350°C, pre-calcination at 650°C, and a calcination step at 900°C for 2h. LCCF was synthesized in exactly the same way, using the respective stoichiometric amounts of the required nitrates of each element: lanthanum nitrate hexahydrate [$La(NO_3)_3 \cdot 6H_2O$; 99,99 %; Alfa Aesar] as a La source, calcium nitrate tetrahydrate [Alfa Aesar, 99 %, $Ca(NO_3)_2 \cdot 4H_2O$] as a Ca source, cobalt nitrate hexahydrate [Alfa Aesar; 98 %, $Co(NO_3)_2 \cdot 6H_2O$] as a Co source, and iron nitrate nonahydrate [Alfa Aesar; 98-101 %; $Fe(NO_3)_3 \cdot 9H_2O$] as an Fe source.

The composition of each cathode powder (e.g. Table 1) was analyzed by inductively coupled plasma optical emission spectrometry (ICP-OES) to verify whether the target composition and stoichiometry was obtained.

Cathode	Target composition	Measured and calculated composition
LSCF	$La_{0.58}Sr_{0.4}Co_{0.2}Fe_{0.8}O_3$	$La_{0.587\pm0.018}Sr_{0.405\pm0.012}Co_{0.202\pm0.006}Fe_{0.787\pm0.024}O_3$
PSCF	$Pr_{0.58}Sr_{0.4}Co_{0.2}Fe_{0.8}O_3$	$Pr_{0.501\pm0.015}Sr_{0.419\pm0.013}Co_{0.15\pm0.006}Fe_{0.845\pm0.025}O_3$
LSC	$La_{0.58}Sr_{0.4}CoO_3$	$La_{0.595\pm0.018}Sr_{0.404\pm0.012}Co_{0.981\pm0.029}O_3$
LSF	$La_{0.58}Sr_{0.4}FeO_3$	$La_{0.585\pm0.018}Sr_{0.403\pm0.012}Fe_{0.992\pm0.030}O_3$
95S1M3	$(La_{0.9}Sr_{0.1})_{0.95}Fe_{0.7}Mn_{0.3}O_3$	$(La_{0.892\pm0.028}Sr_{0.101\pm0.003})_{0.95}Fe_{0.701\pm0.021}Mn_{0.306\pm0.009}O_3$
95S2M8	$(La_{0.8}Sr_{0.2})_{0.95}Fe_{0.2}Mn_{0.8}O_3$	$(La_{0.852\pm0.026}Sr_{0.193\pm0.006})_{0.95}Fe_{0.192\pm0.006}Mn_{0.765\pm0.023}O_3$
LCCF	$La_{0.58}Ca_{0.4}Co_{0.2}Fe_{0.8}O_3$	$La_{0.581\pm0.017}Ca_{0.394\pm0.012}Co_{0.196\pm0.006}Fe_{0.810\pm0.024}O_3$

Table 1. Cathode composition calculated from the ICP-OES cation element measurements.

For phase analysis, and to validate the successful synthesis of the different cathode materials, crystal structure was determined by powder X-ray diffraction using the Bragg–Brentano configuration (D4 Endeavor, Bruker AXS, Cu $K\alpha_{1,2}$ radiation, $\lambda\alpha=1.5418$ Å).

Furthermore, the high-temperature stability of the investigated cathode materials was characterized by comparing the XRD spectra of the respective raw and sintered cathode materials. To do so, cathode-only pellets were prepared by pressing 2g of cathode powder into 22mm pellets using 5kN for 2 min. The cathode-only pellets were then sintered using the fixed heat treatment program (T<1300°C for 5h) and subsequently analyzed by XRD measurements.

The interaction samples (screen printing of the cathode ink on forsterite green plate) were subjected to the general heat treatment program, which was used for all the different samples: T<1300 °C for 5h.

To simplify the interactions of forsterite with the complex perovskite cathode materials, the respective single oxides – La_2O_3 [Sigma-Aldrich; 99.99%], Co_3O_4 [Fluka; 71%], SrO [Sigma-Aldrich; 99.99%], Pr_6O_{11} [Sigma-Aldrich; 99.99%], Fe_2O_3 [Sigma-Aldrich; ≥99%], CaO [ChemPur; 99.99%], and Mn_3O_4 [Sigma-Aldrich; 97%] – were pressed into double-layered pellets (with the exception of La_2O_3, SrO, and Pr_6O_{11} – these oxides were screen printed on a forsterite substrate) and mixed pellets (1g of forsterite mixed with 1g of the respective single oxide) with forsterite (5kN for 2min, D=8, and 22mm). The two types of pellets were subjected to the standard heat treatment program (T<1300 °C for 5h). Cross sections of the samples were subsequently obtained by embedding in epoxy, grinding, and then polishing with silica suspension. The specimens were sputtered with platinum to ensure sufficient electrical conductivity for investigations with a scanning electron microscope (SEM) (Zeiss Ultra55 with EDX from Oxford Instruments; INCAEnergy400 and Feico Phenom).

The properties of the different cathode inks are listed in Table 2. The particle size was measured using a Horiba LA 950 V2 (Retsch Technology GmbH, Haan, Germany). Viscosity was measured with a rheometer (Anton Paar MCR 301) at a shear rate of 109 s^{-1}.

Cathode	Particle size			Viscosity
	d_{10} [µm]	d_{50} [µm]	d_{90} [µm]	[Pa·s]
LSCF	0.63	0.88	1.21	22.9
PSCF	0.60	0.82	1.10	13.4
LSC	0.61	0.85	1.16	12.7
LSF	0.58	0.77	1.00	13.8
LSFM 95S1M3	0.61	0.88	1.26	11
LSFM 95S2M8	0.60	0.79	1.05	13.8
LCCF	0.40	0.80	2.48	13.3

Table 2. Properties of the different cathode inks, which were screen-printed on the Mg silica support material. Viscosity was measured at a shear rate of 109 s^{-1}. All values are rounded to the second decimal value.

In order to exclude the possible influences of different particle sizes, the difference of the d_{10}, d_{50}, and d_{90} was kept as small as possible among the seven cathode inks. The focus was set to the respective d_{50} value.

In summary, five different sample types were prepared and subsequently analyzed:

i) Cathode-only pellets: 2g of the respective cathode powder pressed into pellets

ii) Cathode forsterite: screen-printed cathode inks on forsterite green plates

iii) Cathode mixed pellets: 1g of cathode powder mixed with 1g of forsterite powder

iv) Oxide double-layered pellets: 1g pre-pressed forsterite powder filled with 1g single oxide powder and pressed

v) Oxide mixed pellets: 1g of the respective single oxide powder mixed with 1g of forsterite powder

3 Results

Based on the obtained results, and for a better overview, the seven cathode materials can be subdivided into two types: First, LSCF, LSC, LSF, PSCF and LCCF as they optically exhibit the same interaction behavior with forsterite. Second, both LSFM compositions exhibit similar behavior. For this reason, only one stoichiometric LSFM is shown in the following analysis (SEM of the second LSFM please refer to Supplementary 2).

3.1 *High-temperature stability of the cathode materials*

The high-temperature stability of the investigated cathode materials plays a crucial role in the formation of foreign phases, as the single cathode materials might also decompose at high temperatures (T<1300 °C) leading to the formation of foreign phases.

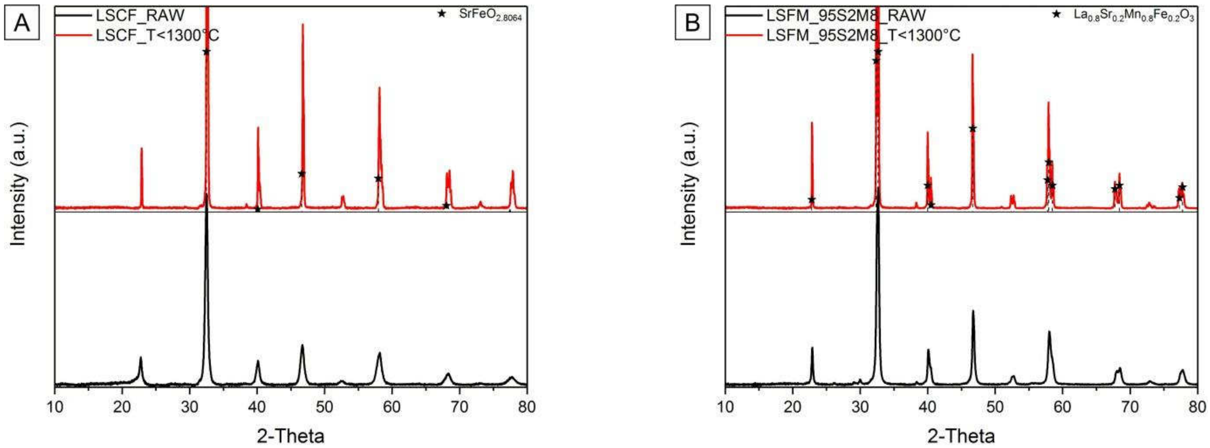

Figure 1: XRD for (A) LSCF raw and LSCF-only pellet and (B) LSFM 95S2M8 raw and LSFM 95S2M8-only pellet. The comparison shows that LSCF does not exhibit high-temperature stability and starts to decompose at higher temperatures. The other diffractograms are displayed in Supplementary 1.

In Figure 1, two diffractograms can be seen – at the bottom of the graph, the cathode raw material is depicted in black; in the upper part of the graph, the sintered cathode-only pellet is highlighted in red. In general, the raw and sintered diffractogram do not show any significant differences. Upon closer inspection of each cathode material, slight changes are visible in the sintered diffractograms.

For the LSCF-only pellet, a foreign phase – which can be attributed to $SrFeO_{2.8064}$ – is visible, indicating the start of LSCF decomposition. In contrast, the LSFM 95S2M8-only pellet (Figure 5B) exhibits stable behavior at T<1300 °C, with only the red spectra being attributed to $La_{0.8}Sr_{0.2}Mn_{0.8}Fe_{0.2}O_3$.

This measurement was performed for all examined cathode materials. It is interesting to note that both the PSCF-only cathode and the LSCF-only cathode decompose by forming Sr–Fe-rich phases: Sr_2FeO_4 and $SrFeO_{2.8064}$. In addition, LSC, LCCF, and LSFM 95S1M3 form secondary phases at high temperatures, which can be attributed to La($CoO_{2.934}$), La($Co_{0.5}Fe_{0.5}O_3$), and $LaFeO_3$, respectively. These findings are supported by Stevenson et al. [42], as the authors examined the stability of different LSCF and LCCF compositions, and found that the stability of perovskites with high contents of Sr and Co are very limited. Only LSF and LSFM 95S2M8 exhibit stable behavior at T<1300°C, since only ($La_{0.6}Sr_{0.4}$)FeO_3 and $La_{0.8}Sr_{0.2}Mn_{0.8}Fe_{0.2}O_3$ were detected within the XRD diffractograms. It is therefore only these two cathodes that can be described as “X-ray phase-pure” after heat treatment.

3.2 SEM characterization

The interactions of the different cathode materials with the forsterite support provide an initial overview of the reaction tendency. For this study, the cathode–forsterite samples were analyzed. For this study the particle size of the inks were not kept constant, that’s why no further analytics concerning the porosity visible in the following figures were performed.

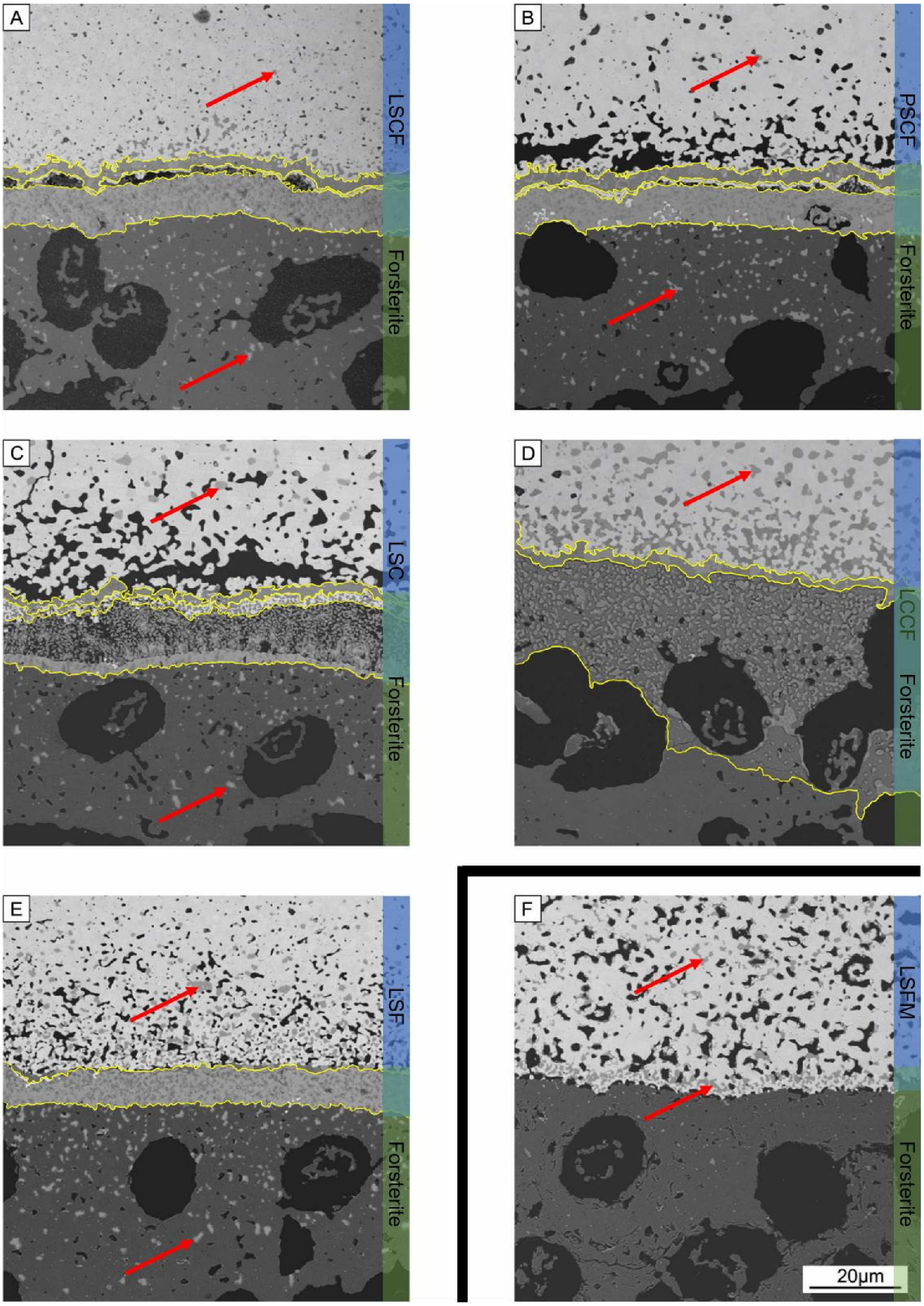

Figure 2: SEM cross sections after screen printing of cathode–forsterite samples with: (A) LSCF, (B) PSCF, (C) LSC, (D) LCCF, (E) LSF, and (F) LSFM 95S2M8 on forsterite. For (A)-(E), the cross sections show a very strong reaction and the formation of reaction layers. In contrast, (F) shows only some foreign phases. Reaction layers are highlighted in yellow; foreign phases indicated with a red arrow.

Figure 2 shows the interaction of the different cathodes with forsterite. Cathodes A–E display a strong tendency to react with forsterite. Thick and thin reaction layers are visible (denoted by yellow lines) as well as several foreign phases (red arrows). In contrast, the LSFM in Figure 2F only shows the formation of some foreign phases and does not display the same strong tendency to react with forsterite. LSCF-forsterite (Figure 2A) reveals the formation of two reaction layers with averaged thicknesses of 6.5µm and 3µm, respectively. Furthermore, the foreign phases are distributed inside the LSCF and the support. PSCF–forsterite (Figure 2B) exhibits the same behavior as LSCF–forsterite: several foreign phases and two reaction layers with thicknesses of 6.7µm and 2.6µm – which is in the same range as LSCF–forsterite – are formed after heat treatment. LSC–forsterite and LCCF–forsterite (Figure 2C and 1D) also form two reaction layers with thicknesses of 9µm and 2.3µm, and 30µm and 1.8µm, respectively. For both systems, the thick reaction layer appears to become softer as it is peeled off during grinding and polishing of the embedded cross-section samples. In comparison to the four aforementioned cathode materials, LSF–forsterite (Figure 2E) only shows the formation of one single reaction layer with a thickness of 5.8µm.

In contrast to cathodes (A)–(E), no reaction layer is visible for LSFM 95S2M8 (F). However, as with all cathode materials, the formation of foreign phases is observed, which are spread all over the cathode and support (higher concentration at the interface). The very same observation was made for LSFM 95S1M3. This had been expected, since the compositions only show slight differences. For this reason, the cross section of LSFM 95S1M3 is not shown from Figure 2 (see Supplementary 2).

3.3 *Qualitative diffusivity of the different elements: EDX/WDX*

As can be seen in Figure 2, all the cathode materials exhibit a certain reactivity with forsterite, forming several foreign phases and/or reaction layers. In order to gain further insight into the diffusion tendency of the different cathode and forsterite elements, energy-dispersive X-ray spectroscopy (EDX) was performed on the embedded, grinded, and polished cathode–forsterite samples. As the EDX signal overlaps for Si and Sr (at 1.74 keV and 1.81 keV, respectively), wavelength-dispersive X-ray (WDX) measurements were performed to separate these elements. For a better overview, Figure 3 only displays the signals for the LSCF–forsterite sample. Additional EDX point scans for LSCF-forsterite are displayed in Supplementary 4.

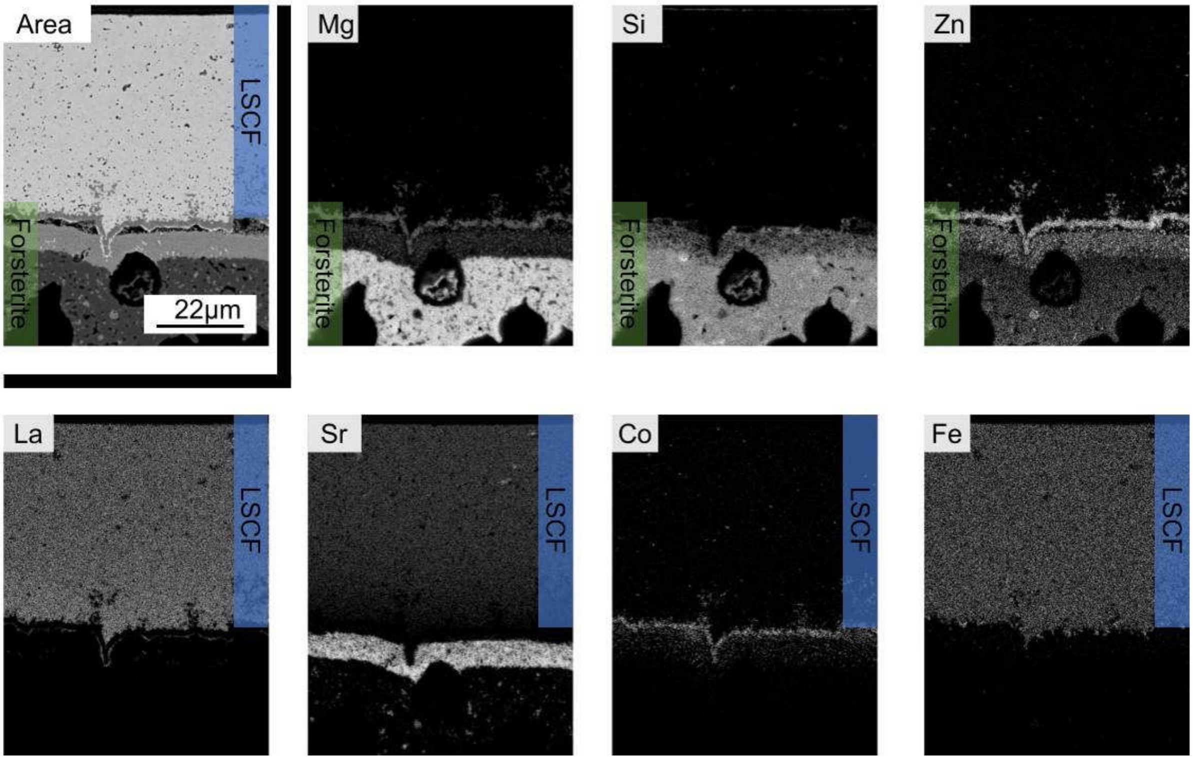

Figure 3: EDX (Mg, Zn, La, Co, and Fe) and WDX (Si and Sr) mapping from LSCF–forsterite. The brightness is correlated to the concentration of the elements. Regions appearing as black do not contain any traces of the respective element

Alongside the cross section, the major elements of the support material forsterite (highlighted in green) are displayed: Mg, Si, and Zn (excluding Ca). At the bottom of Figure 3, the respective elements of the LSCF cathode (highlighted in blue) are listed: La, Sr, Co, and Fe. Similar to Figure 2A, Figure 3 shows that LSCF–forsterite forms two reaction layers and several foreign phases within the forsterite and LSCF.

With respect to the elements of forsterite, a diffusion gradient is visible. The signals of Mg, Zn, and Si become less visible with increasing distance from the forsterite. For example, Mg concentration gradient shows that Mg is involved in the formation of the two reaction layers. However, the majority of Mg remains inside the support material itself and does not diffuse strongly into the LSCF. In contrast, the foreign phases close to the thin reaction layer contain small amounts of Mg. The same trend is observed for Zn, although Zn displays a stronger diffusion tendency, as the entire cathode (50µm thick) shows some Zn signals and Zn-rich foreign phases. In addition, the majority of Zn appears to be located inside the thin reaction layer. Si exhibits the same behavior with respect to the foreign phases, the depth of diffusion into the LSCF, and the formation of the thick reaction layer. One noticeable difference, however, is that Si cannot be detected within the thin reaction layer.

In terms of the elements of LSCF – La, Sr, Co, and Fe – only La hardly diffuses. The La signal is only visible inside the cathode layer and beneath the thin reaction layer. In contrast, Fe, Co, and Sr (in ascending order) exhibit a certain diffusion towards the support material forsterite.

Inside the support material, there is a lack of a Fe signal, which can only be obtained inside the cathode material and the thick reaction layer. Co and Sr, meanwhile, exhibit strong diffusion. Co shows an enrichment within the thin and the thick reaction layers, although this results in the depletion of Co inside the cathode. A similar behavior is observed for Sr, which is abundant inside the thick reaction layer and the foreign phases inside the support material. Only the thin reaction layer displays a lack of Sr. Classification of the elements to a crystallographic phase follows in section 3.4.

To summarize the EDX and WDX mappings for LSCF–forsterite, the cathode side layer mostly contains Ca, Co, Fe, Mg, and Zn. The support side layer consists of Sr, Si, Ca, Co, Mg, and Zn. Foreign phases, which can be found in the cathode and the support, contain Sr, Si, Ca, Co, Mg, Zn, La, and Fe, as well as Sr, Si, Mg, Zn, and Fe respectively. These tests were performed for all cathode–forsterite combinations. Based on these findings as well as further EDX point scans and mappings, the diffusion tendency of each element for all reaction partners can be qualitatively visualized in a simplified scheme, as shown in Figure 4.

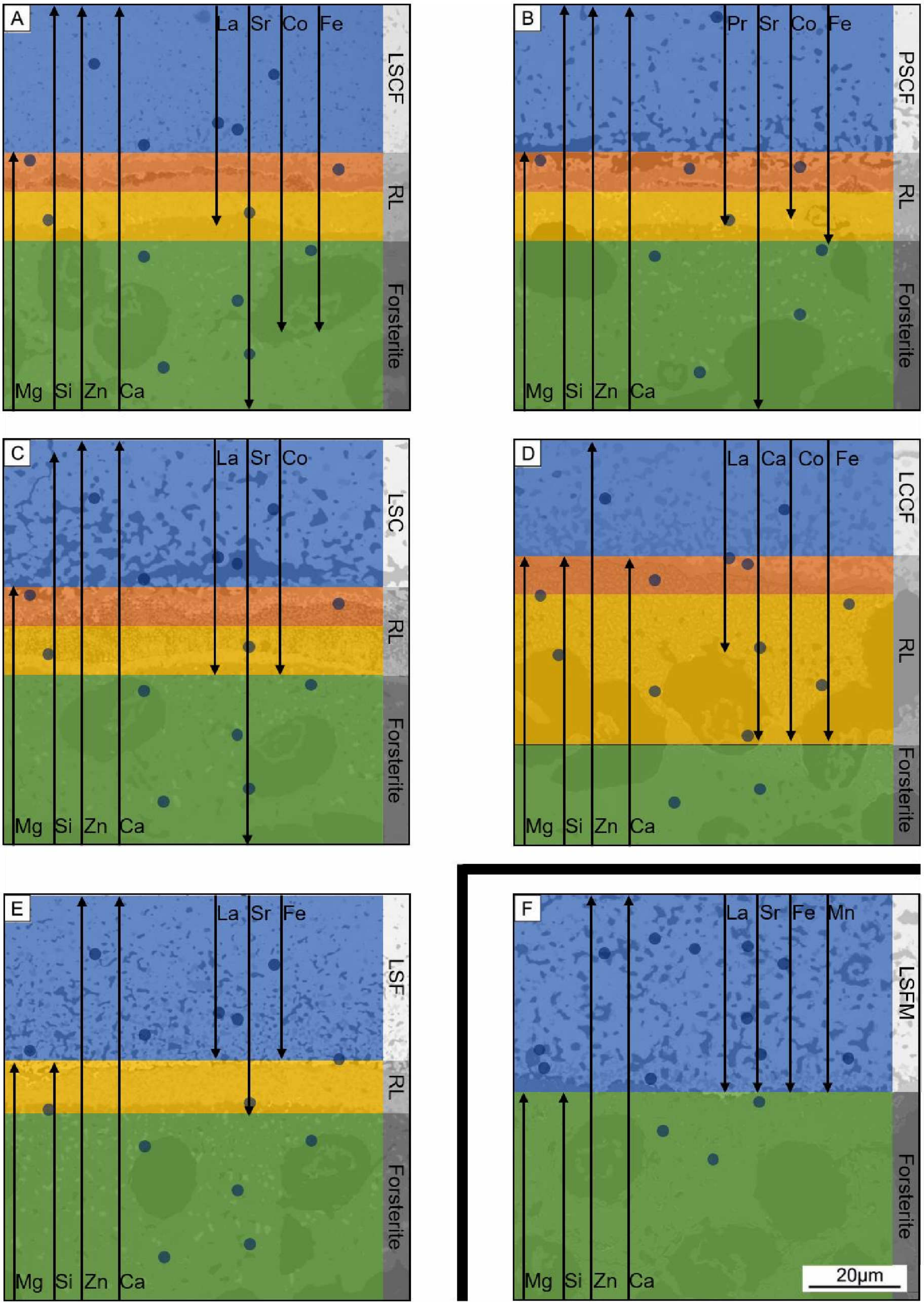

Figure 4: Diffusion tendency of each element for the respective cathode–forsterite system for: (A) LSCF, (B) PSCF, (C) LSC, (D) LCCF, (E) LSF, and (F) LSFM 95S2M8. With respect to the support material, Zn and Ca show the greatest diffusion followed by Mg and Si.

Figure 4 visualizes the diffusion depth of each element. Mg, Si, Zn, and Ca originate from the support (highlighted in green). The elements from the respective cathodes, for example La, Sr, Co, and Fe, originate from the top (highlighted in blue). At the interface, reaction layers are formed (thin reaction layer highlighted in dark orange; thick reaction layer highlighted in yellow and designated “RL”). The blue dots inside the respective schemes indicate the formation of foreign phases.

In terms of the cathode elements, La and Pr never diffuse inside the support material. The maximum diffusion depth is limited to the interface and/or reaction layer. For the Sr-containing cathodes, Sr can be identified as the most diffusing element. With the exception of LSCF, Co, Fe, and Mn exhibit similar behavior: they do not diffuse into the support material.

Mg never diffuses from the support material, forsterite, into the cathode material. Si exhibits a strong reaction tendency, as it is mostly found inside the reaction layers. Zn and Ca diffuse the most (except for LCCF), with the entire cathode material showing a certain Zn and Ca signal. However, the majority of Zn and Ca is located inside the reaction layers and foreign phases.

For all cathode–forsterite combinations, Sr, Si, Zn, and Ca can be identified as the most diffusing elements. These are followed by Co, Fe, and Mn. However, La and Pr do not diffuse into the support material and are not really involved in the formation of reaction layers and foreign phases.

3.4 *Phase analysis after heat treatment: XRD*

Several foreign phases and reaction phases are formed after sintering each cathode–forsterite combination. For a more precise quantification of these phases, XRD measurements were performed for each cathode–forsterite combination. This was carried out for the cathode mixed pellets.

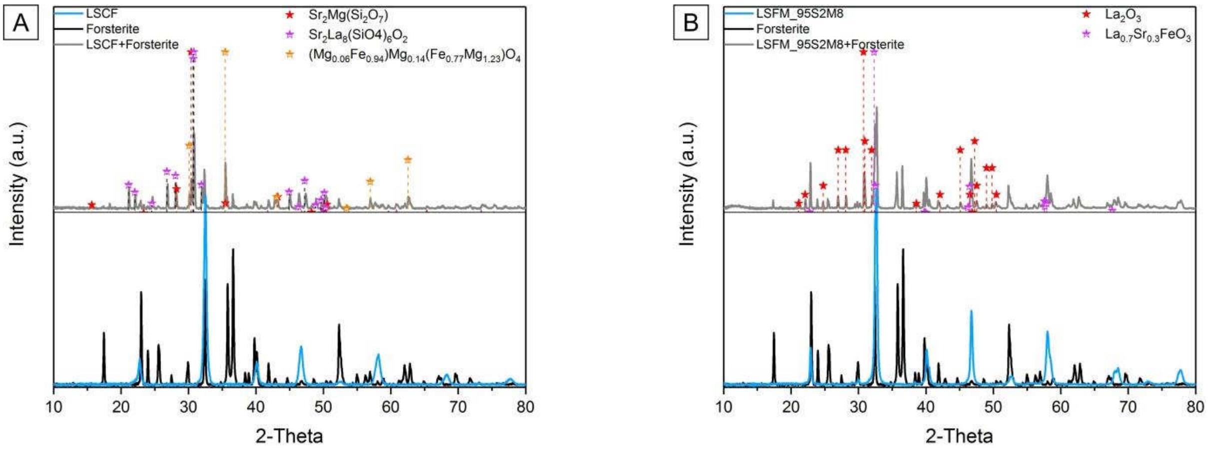

Figure 5: XRD for (A) LSCF–forsterite and (B) LSFM 95S2M8–forsterite (in grey; mixed pellet) after T<1300 °C 5h. The spectra are shown for raw forsterite (black line) and for the raw cathode material (blue line).

Figure 5 displays three different spectra. At the bottom of the graph, the respective diffractogram of the cathode raw material and forsterite raw material are highlighted in blue and black, respectively. In the upper part of the graph, the cathode mixed pellet of the respective cathode and forsterite sintered at T<1300 °C for 5h is depicted in grey. After sintering, several foreign phases are formed and can be identified (denoted by stars).

The XRD measurement underlines the findings of the EDX and WDX measurements: Sr-rich phases are formed during heat treatment. For LSCF–forsterite, the foreign phases can be attributed to $Sr_2Mg(Si_2O_7)$, $Sr_2La_8(SiO_4)_6O_2$, and $(Mg_{0.06}Fe_{0.94})Mg_{0.14}(Fe_{0.77}Mg_{1.23})O_4$. For LSFM 95S2M8–forsterite they can be attributed to La_2O_3 and $La_{0.7}Sr_{0.3}FeO_3$.

PSCF–forsterite shows the same phases as LSCF–forsterite with the exception of $Sr_2Pr_8(SiO_4)_6O_2$, as PSCF does not contain any La (cf. Supplementary 3). These findings are in good agreement with the SEM cross sections, since PSCF–forsterite and LSCF–forsterite exhibit identical interface (cf. Figure 2). The following table lists the other cathode-forsterite combinations and their respective formed foreign phases after the standard heat-treatment.

Cathode-forsterite	Foreign phases formed			
LSF-forsterite	Ca_2SiO_4	SiO_2	$Sr_2Mg(Si_2O_7)$	$ZnFe_2O_4$
LSC-forsterite	Sr_2Si	$SrSi_2$	$Co_{1.76}Zn_{13.24}$	
LCCF-forsterite	$Ca_3Mg(SiO_4)_2$	$CaLa_4(SiO_4)_3O$		
LSFM 95S1M3-forsterite	Fe_3O_4	$La_{9.33}(Si_6O_{26})$		

Table 3: Cathode-forsterite combinations and their formed phases after the standard heat-treatment. The spectra are shown in the supplementary section (cf. Supplementary 3).

The majority of the foreign phases contain Sr and Si. Furthermore, based on the EDX and WDX mappings (cf. Figure 3 and Figure 4), the cathode–forsterite combinations are also expected to form more phases containing Zn. However, with the XRD measurements, this was only observed for LSF–forsterite, probably because of the small amount of Zn compared to Si. In addition, the EDX and WDX mappings demonstrated that La and Pr do not tend to be involved in the formation of foreign phases. This was underlined by the XRD measurements, as most of the phases detected by XRD did not contain La or Pr.

3.5 Reactivity of different oxides with the support material: EDX and XRD

In order to attribute the strong reaction of forsterite to a single element visible in figure 2, individual oxide interaction tests were performed with La_2O_3, Co_3O_4, SrO, Pr_6O_{11}, Fe_2O_3, CaO, and Mn_3O_4 as basic oxides for the perovskites.

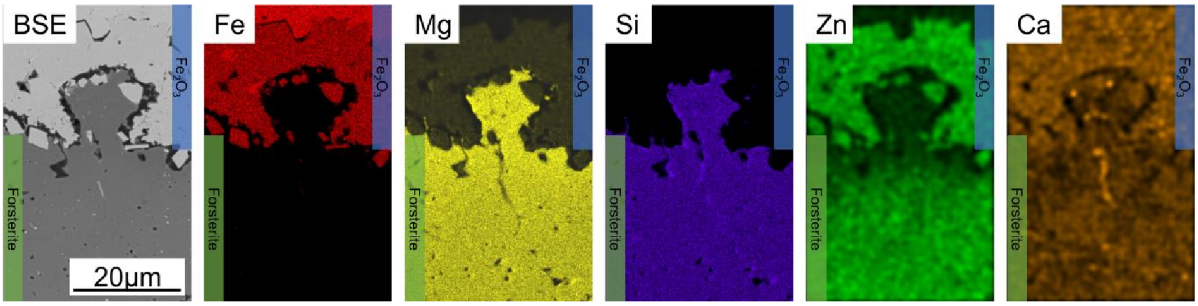

Figure 6: EDX mapping of the oxide double-layered pellet sample: Fe_2O_3 double-layered pellet. Two layers are visible. They differ considerably with respect to their Mg and Zn content, which is visualized by the EDX mapping.

The EDX mapping for Fe_2O_3 double-layered pellet (Figure 6) shows the formation of two reaction layers after heat treatment, which are comparable to the two reaction layers visible for LSCF–forsterite (Figure 2A). In addition, the majority of Zn and Ca is again found within this reaction layer. The reaction layers of the Fe_2O_3 double-layered pellet contain Ca, Mg, Zn, and Fe, and Ca, Zn, and Fe, respectively.

A certain diffusion of the different elements is also observed for all the other single oxides (cf. Supplementary 5).

An analysis of the oxide double-layered pellets lead to the same conclusion as the one from the cathode–forsterite combinations: Zn and Ca are distributed across the whole oxide each time. These findings are supported by Matte et al. [18]. However, the tendency for La_2O_3 and Pr_6O_{11} to react with forsterite appears to be very limited.

The strong diffusion of Zn and Ca from the not finally densified pellets leads to the assumption that these elements are not only distributed by solid-state diffusion, but also via gas diffusion.

In order to validate these results, additional XRD measurements were performed.

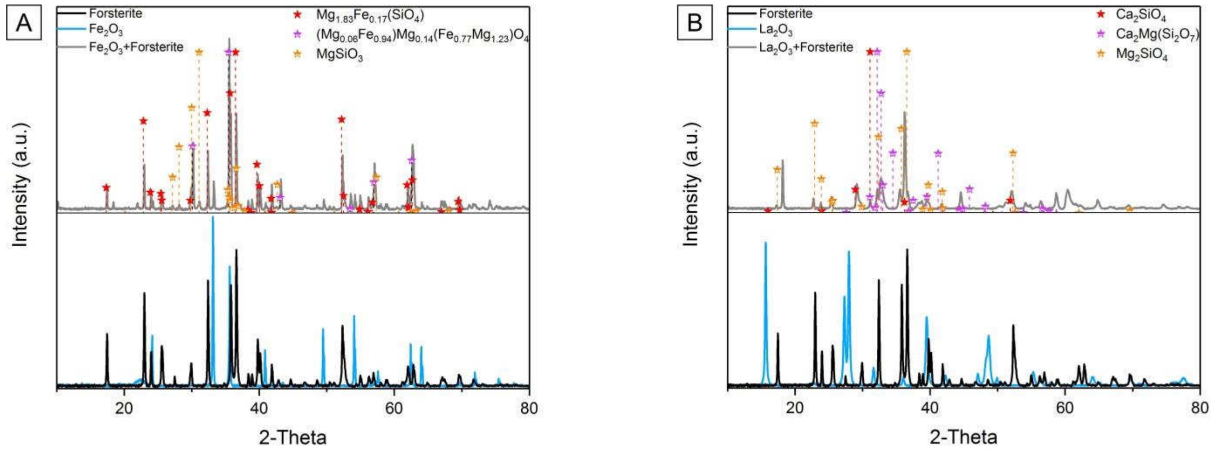

Figure 7: XRD measurement of oxide mixed pellets for (A) Fe_2O_3 mixed pellets and (B) La_2O_3 mixed pellets. The resulting reaction phases are depicted in the figure for intensities greater than 10%.

Figure 7 shows three different diffractograms: At the bottom of the graph, the diffractogram of the individual oxide raw material and the forsterite raw material are depicted in blue and black, respectively. In the upper part of the graph, the oxide mixed pellet of the respective oxide and forsterite sintered at T<1300°C for 5h is highlighted in grey. After sintering, several foreign phases are formed and can be identified (denoted by stars).

The XRD measurements, summed up in Table 4, serve to underline the formation of reaction phases for Fe_2O_3, SrO, Mn_3O_4, Co_3O_4, and CaO (cf. Supplementary 6).

Mixed-pellets	Foreign phases formed		
Fe_2O_3	$(Mg_{0.06}Fe_{0.94})Mg_{0.14}(Fe_{0.77}Mg_{1.23})O_4$	$Mg_{1.83}Fe_{0.17}(SiO_4)$	$MgSiO_3$
SrO	Sr_2SiO_4	$Sr_3MgSi_2O_8$	$Sr_3O(SiO_4)$
Mn_3O_4	$Ca_3(SiO_3)_3$	$MgMnSi_2O_6$	$Mn_{11}Si_{19}$
Co_3O_4	$(Co_{0.175}Mg_{0.825})_2(SiO_4)$	MgO	
CaO	Ca_2SiO_4	$Ca_3Mg(SiO_4)_2$	MgO

Table 4. Listing of the different oxide mixed-pellets and their respective foreign phases formed with forsterite after the standard heat-treatment.

With these oxides, the foreign phases that are formed contain Mg and/or Si, thereby underlining the reactivity of Mg and Si from the forsterite support material. Despite the reaction tendency of the listed single oxides with forsterite, Figure 7B shows that La_2O_3 does not tend to react with forsterite, since the phases formed after heat treatment do not contain La. The same observation was made for Pr_6O_{11}: No reaction phase is formed with Pr (cf. Supplementary 6). These findings are in good agreement with the results obtained from EDX and WDX cathode–forsterite combinations (cf. Figure 3 and Figure 4).

4 Discussion

All cathode–forsterite combinations exhibit a certain reaction. With the exception of the two LSFM stoichiometries, all the cathode materials result in the formation of a reaction layer. Further information on these cathode–forsterite combinations is given in Table 5.

Cathode	Substrate side		Cathode side	
	[µm]	Composition	[µm]	Composition
LSF–forsterite	5.8	Sr Si Ca Mg Zn		
LSCF–forsterite	6.5	Sr Si Ca Co Mg Zn	3	Ca Co Fe Mg Zn
PSCF–forsterite	6.7	Sr Si Ca Co Mg Zn	2.6	Ca Co Fe Mg Zn
LSC–forsterite	9	Sr Si Ca Co Mg Zn	2.3	Ca Co Mg Zn Si Sr
LCCF–forsterite	30	Si Ca Co Mg Zn	1.8	Co Fe Mg Zn

Table 5. Reaction layers of cathode–forsterite combinations: LSF, LSCF, PSCF, LSC, and LCCF, and their respective elemental compositions. In terms of the thickness of the layer, the mean value of ten measurements was used. The elemental composition was analyzed by EDX measurements.

Table 5 provides an overview of the cathodes forming a reaction layer with forsterite after heat treatment at T<1300°C for 5h (cf. Figure 2A–E). Interestingly, the substrate side and the cathode side reactions layer mostly contain the same elements: Sr-Si-Ca-Co-Mg-Zn and Ca-Co-Mg-Zn-Fe, respectively. Comparing these results with the two LSFM cathodes – which only display several foreign phases mostly consisting of Si-Sr-Zn – underlines the strong reactivity of Si, Sr, and Zn. These results are in good agreement with the literature. [18] Furthermore, La and Pr from the A-site of the respective perovskite materials do not show any tendency to react with forsterite. These results are supported by the individual oxide measurements (cf. Figure 7 and Supplementary 6) as well as by the EDX mappings of the double-layered single oxide pellets of La_2O_3 and Pr_6O_{11} with forsterite (cf. Figure 6 and Supplementary 5). These tests were performed to identify elements that do not react with the support material. The findings from these EDX mappings and XRD measurements demonstrate the non-reactivity of La_2O_3 and Pr_6O_{11}, since there is no foreign phase or any reaction layer present after heat treatment at T<1300°C for 5h. In terms of the other oxides, the foreign phases which can be found for the SrO, CaO, Mn_3O_4, and Co_3O_4 oxide mixed pellet combinations all contain Sr and/or Mg.

During heat treatment, Sr segregation occurs for A-site Sr-rich perovskites. [43] As all of the examined cathode materials already display a certain A-site deficiency (2–5%), Sr-segregation further enhances the A-site deficiency, which results in a collapse of the B-site. This assumption is supported by the optical properties of the cathode-only pellets after sintering at T<1300°C for 5h. All of the samples displayed a broad blue circle on the Al_2O_3 sintering plate, indicating the formation of an Al–Co spinel.

Furthermore, the literature [43-46] states that oxygen gradients can cause faster B-site elemental diffusion, supporting the assumption of B- and A-site decomposition. These “free” elements are prone to react with the support material forsterite and to form foreign phases and reaction layers mostly containing Sr, Co, and Fe from the cathode as well as Mg, Si, Zn, and Ca from the support material

This assumption is supported by the XRD measurements of the respective cathode materials after synthesis and heat treatment at T<1300°C (cf. Section 3.4). However, no decomposition was observed for LSF [43] and LSFM 95S2M8, indicating that it is not just the decomposition of the respective cathode materials responsible for the formation of new phases and reaction layers. In the literature, cation mobility – due to gradients within the examined material – at high temperatures is given as one possible reason for the demixing and decomposition [44, 46], ultimately resulting in the formation of new phases.

With regard to forsterite and doping with different elements, the tendency of forsterite to incorporate different elements inside the olivine structure is highlighted by Gheitaschi et al. [28]. The authors underline the reactivity of Sr and forsterite. Excess Sr leads to the formation of $Sr_2MgSi_2O_7$. The exact same phase was obtained for the cathode–forsterite mixture of LSCF, LSF, and PSCF.

The strong reactivity of Sr and Si was further investigated by screen printing SrO on forsterite. After sintering, the XRD and EDX measurements revealed that all of the phases which were formed contained Sr, Si, and Mg (cf. Gheitaschi et al. [28]).

In summary of the different influences most likely to lead to the formation of foreign phases and reaction layers, the following processes must be highlighted:

a) High-temperature stability of perovskite

The cathode materials used in this publication are all dependent on the crystal structure of the perovskite materials. To maintain a high oxygen–anion exchange, the cathodes exhibit an A-site deficiency of 2% or 5%. However, this thermodynamic state is not stable at high temperatures, resulting in the decomposition of the cathode material at a certain temperature, which in turn leads to the formation of different phases with a lower bond enthalpy compared to the perovskite (cf. Figure 1).

b) Concentration gradient

The diffusion of elements can be due to several reasons, such as thermal, electrical, chemical, or chemical potential gradients. [43, 45] Taking this into account, the elements of the support material and the elements of the respective cathode materials for each cathode–forsterite combination attempt to achieve a stable state. This leads to the interdiffusion of elements from the support towards the cathode and vice versa. As displayed in the diffusion depth schematic, figure 4 shows that within a time range of 5h at $T<1300°C$, certain elements are more prone to diffusion than others (cf. Zn and Ca vs. La and Pr). These findings are supported by Matte et al. [18]

c) Sr segregation

It is known from the literature that Sr segregation occurs in perovskite materials with a high Sr content. [47] This segregation of Sr promotes the formation of Sr-rich phases.

5 Conclusion

Using forsterite as a support material for SOFC applications is a promising way of achieving a low-cost SOFC, since forsterite supports the co-firing of all functional layers. However, the seven different cathode materials examined tend to react with forsterite. Several foreign phases and reaction layers can thus be observed. The thicknesses of these reaction layers averages between 1.8µm and 30µm. The two LSFM compositions do not show any reaction layer. However, many different foreign phases are found within the cathode itself and the support material forsterite. These findings were analyzed by SEM, XRD, EDX, and WDX measurements, which revealed that Si, Sr, and Zn are mostly responsible for the formation of the reaction layers and foreign phases. With XRD, EDX, and WDX measurements, La and Pr were identified as elements that did not react with forsterite after heat treatment of the respective oxide, double-layered and mixed pellets, and the perovskite materials containing either La or Pr at T<1300°C for 5h. In addition, the analysis demonstrated that Zn and Ca are the most diffusing elements in the examined cathode–forsterite combinations.

Furthermore, the reactivities of LSCF, LSC, PSCF, LCCF, and LSFM 95S1M3 with forsterite can be attributed to the decomposition of these perovskite materials at T<1300°C. These findings are supported by XRD measurements, in which only LSF and LSFM 95S2M8 were identified as cathode materials exhibiting high-temperature stability. The results indicate that an SOFC system with forsterite as a support material should utilize a cathode excluding Sr, Co, Fe, Ca, and Mn. The question arises as to how these foreign phases and reaction layers affect the electrocatalytic activity of the investigated cathode materials. The influence of phase formation and interdiffusion phenomena will be discussed in Part 2 of this paper.

Acknowledgement:

The authors would like to thank Dr. Egbert Wessel, Institute of Energy and Climate Research – Microstructure and Properties of Materials (IEK-2), Forschungszentrum Jülich, for conducting EDX and WDX measurements. The authors would also like to thank Dr. Volker Nischwitz, Central Institute of Engineering, Electronics and Analytics – Analytics (ZEA-3), Forschungszentrum Jülich, for performing wet chemical analyses. The project "KerSOLife100" (FKZ: 03ET6101) was funded by the Federal Ministry for Economic Affairs and Energy (BMWi).

6 Supplementary data

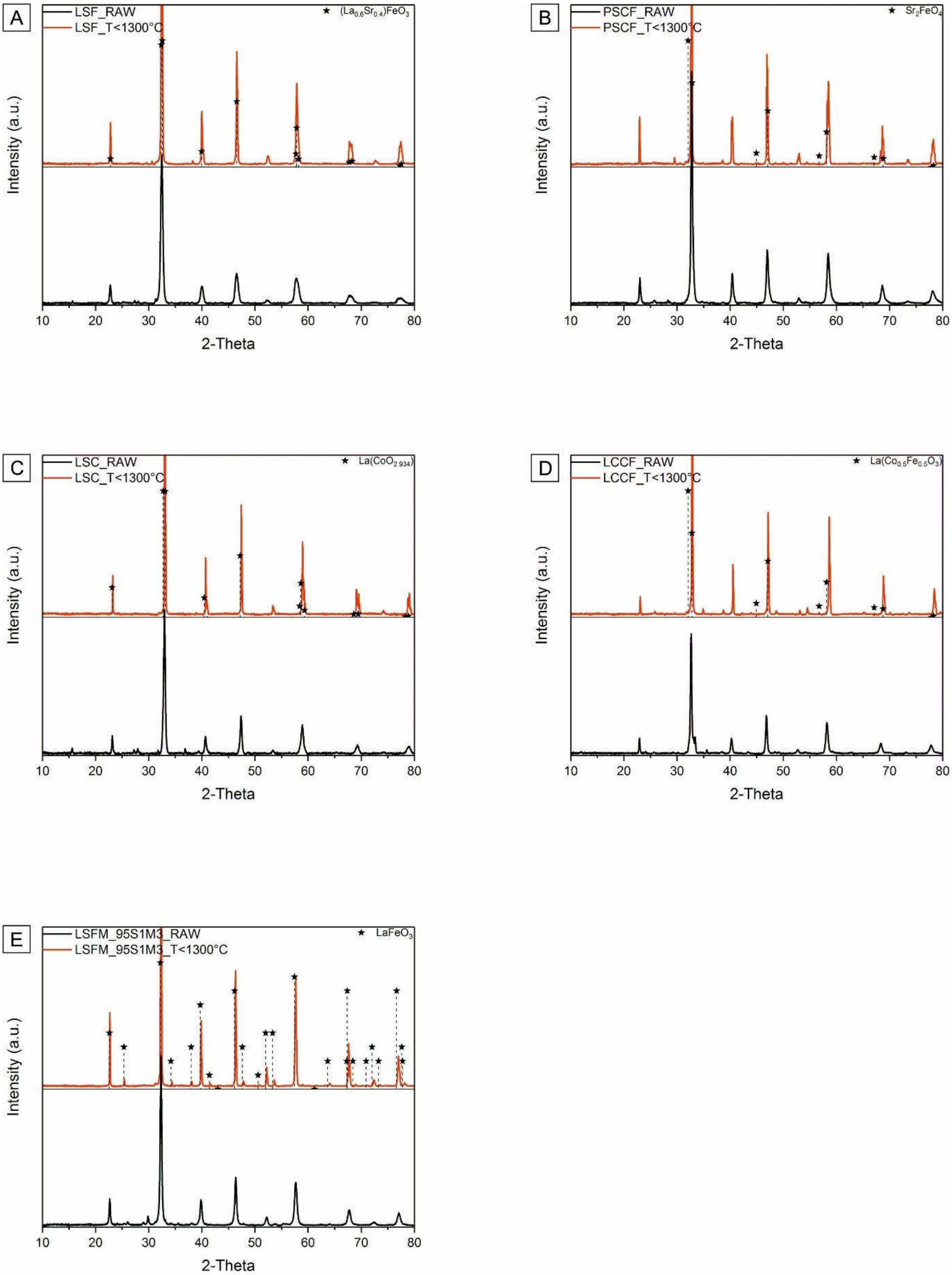

Supplementary 1: XRD of cathode raw and cathode-only pellets for (A) LSF, (B) PSCF, (C) LSC, (D) LCCF, and (E) LSFM 95S1M3.

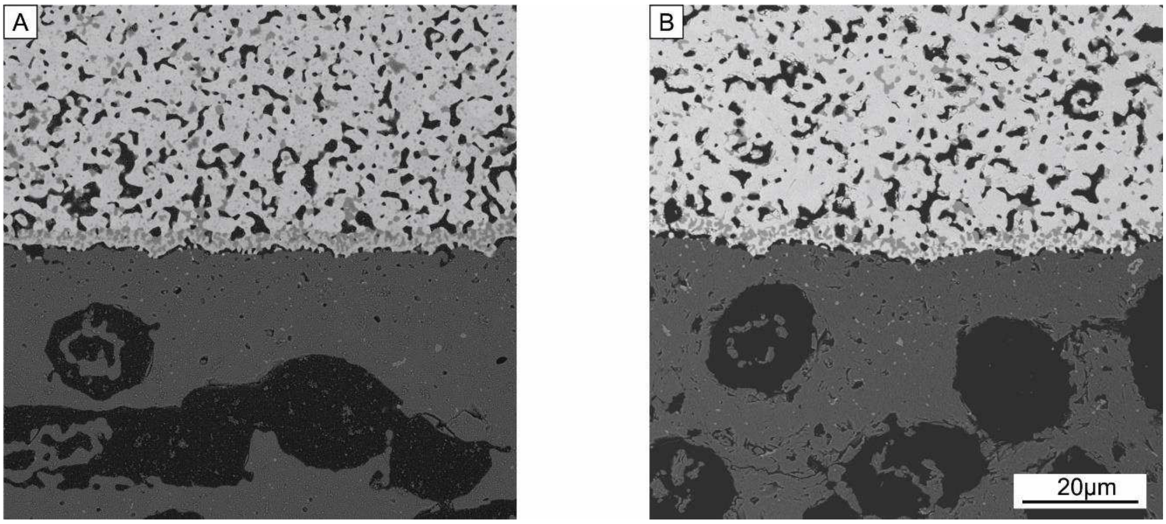

Supplementary 2: Comparison of the SEM cross sections of cathode–forsterite samples for (A) LSFM_95S2M8 and (B) LSFM 95S1M3.

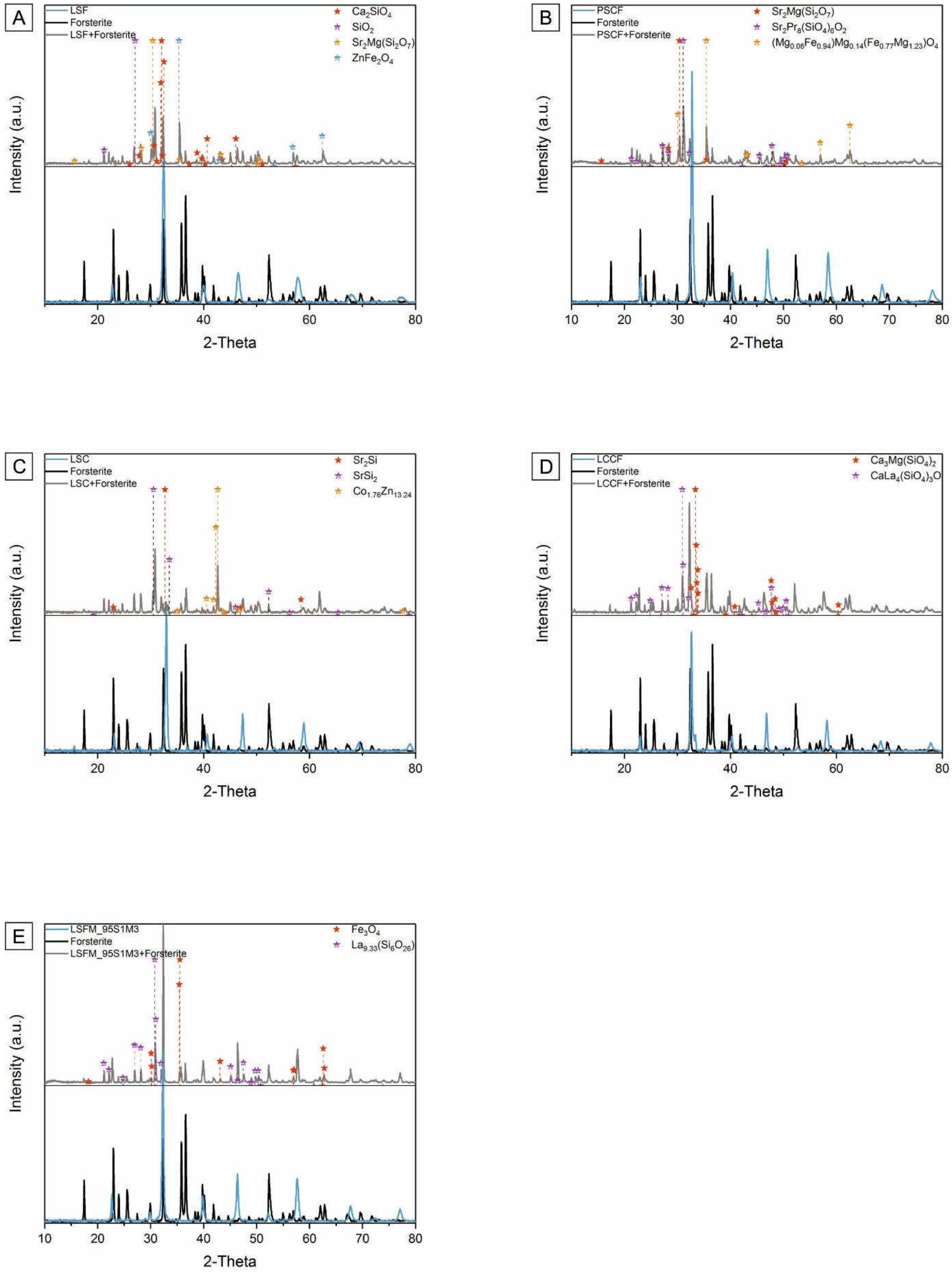

Supplementary 3: XRD of cathode mixed pellets for (A) LSF, (B) PSCF, (C) LSC, (D) LCCF, and (E) LSFM 95S1M3.

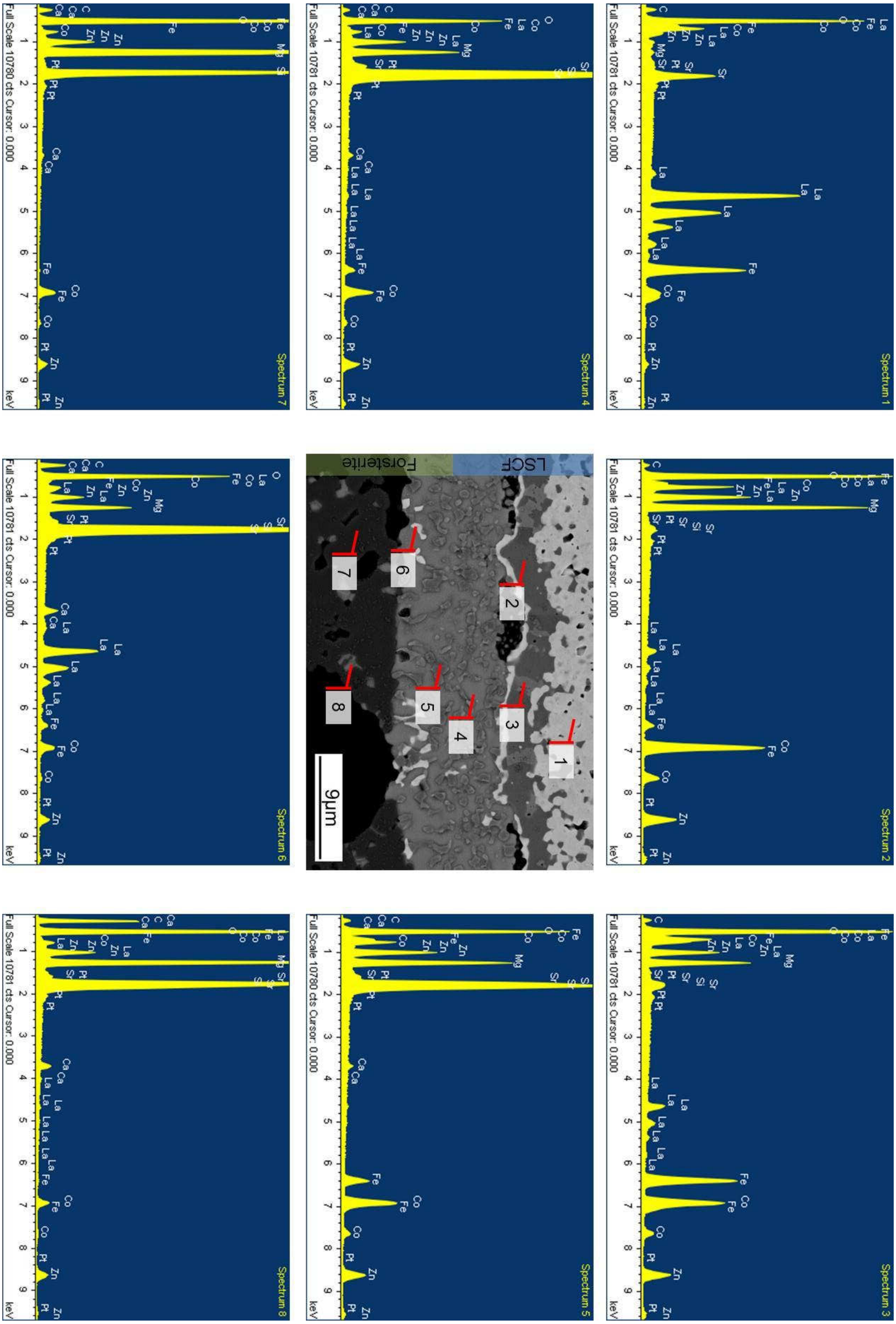

Supplementary 4: EDX Pointscans from LSCF-forsterite. Eight different phases are formed after the standard heat treatment.

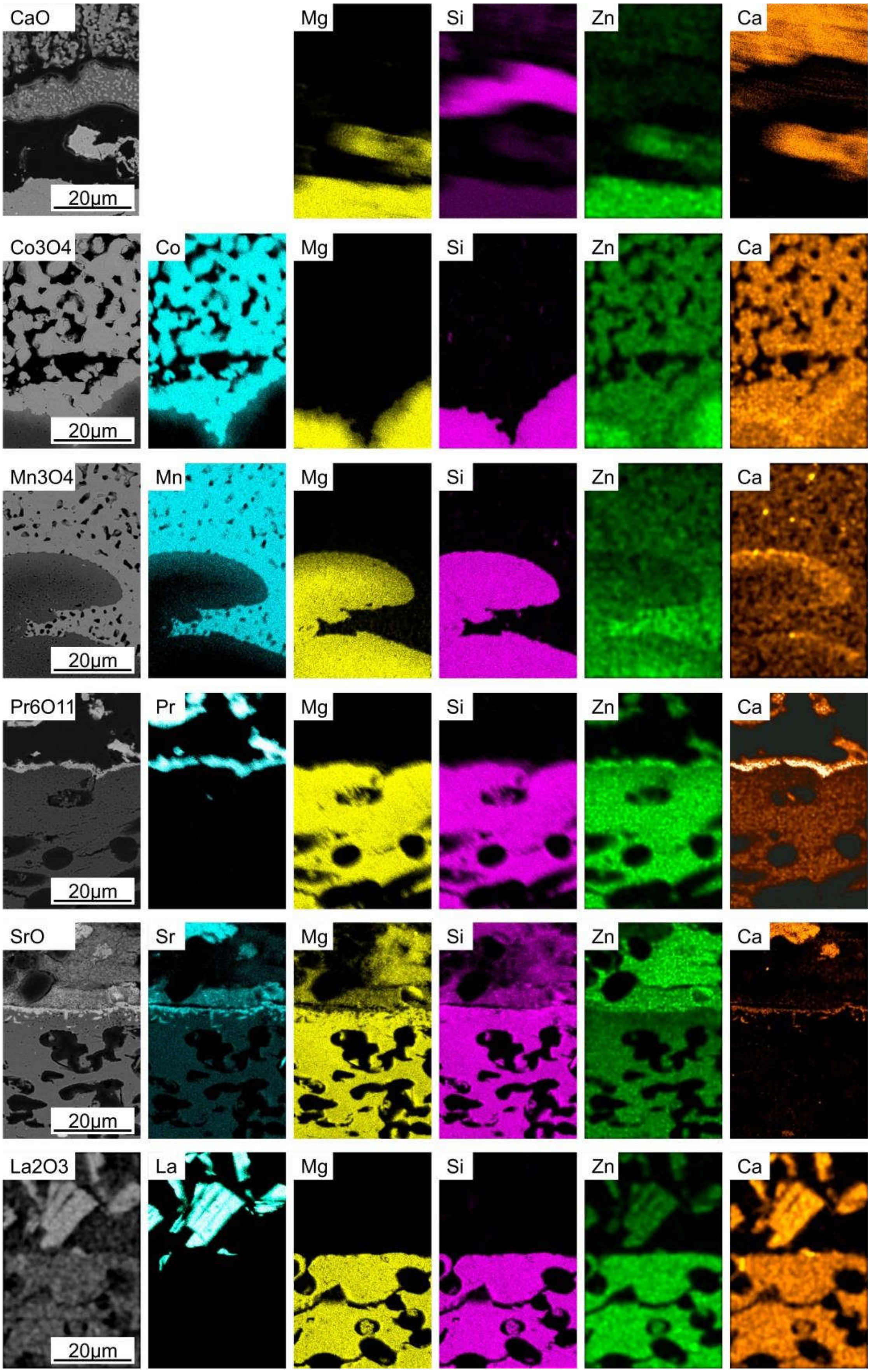

Supplementary 5: EDX mappings of oxide double-layered pellets for CaO, Co_3O_4, Mn_3O_4, Pr_6O_{11}, SrO, and La_2O_3

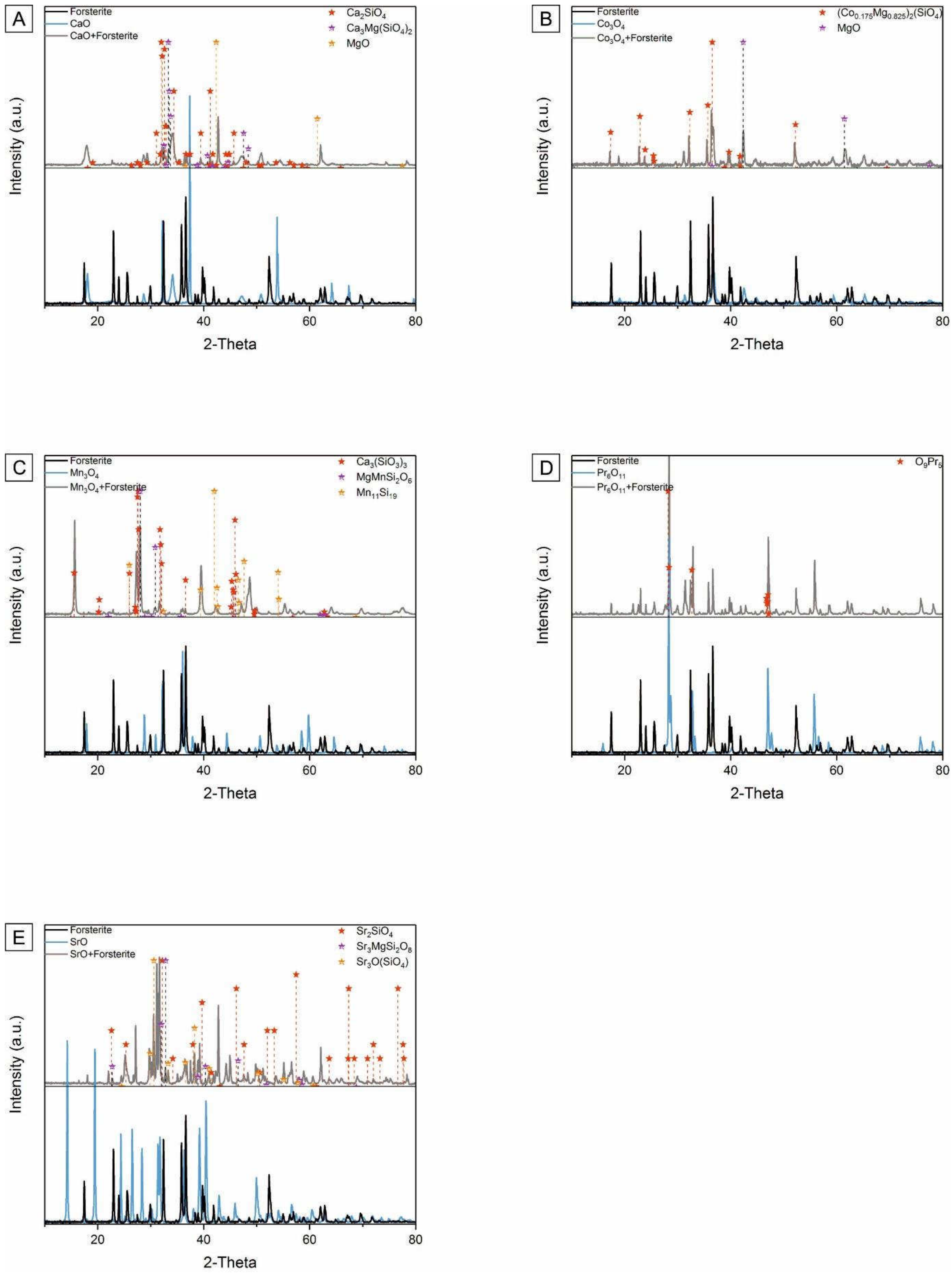

Supplementary 6: XRD measurements of the raw forsterite (black line) and the respective raw single oxides (blue line) of (A) CaO, (B) Co_3O_4, (C) Mn_3O_4, (D) Pr_6O_{11}, and (E) SrO, and the respective oxide mixed pellet combinations (grey line). The respective foreign phases are depicted in the graphic for intensities greater than 10%.

7 References

[1] A.B. Stambouli, E. Traversa, Renewable & Sustainable Energy Reviews, 6 (2002) 295-304.

[2] N.M. Sammes, Fuel cell technology : reaching towards commercialization, Springer, London, 2006.

[3] N.Q. Minh, Journal of the American Ceramic Society, 76 (1993) 563-588.

[4] L. Blum, W.A. Meulenberg, H. Nabielek, R. Steinberger-Wilckens, International Journal of Applied Ceramic Technology, 2 (2005) 482-492.

[5] J.M. Andújar, F. Segura, Renewable and Sustainable Energy Reviews, 13 (2009) 2309-2322.

[6] N.Q. Minh, T. Takahashi, Science and Technology of Ceramic Fuel Cells, Elsevier Science Ltd, Oxford, 1995.

[7] N. Menzler, FUEL CELLS, 14 (2014) 96-106.

[8] N.H. Menzler, F. Tietz, S. Uhlenbruck, H.P. Buchkremer, D. Stover, Journal of Materials Science, 45 (2010) 3109-3135.

[9] N.H. Menzler, W. Schafbauer, F. Han, O. Buchler, R. Mucke, H.P. Buchkremer, D. Stover, Development of High Power Density Solid Oxide Fuel Cells (SOFCs) for Long-Term Operation, in: J.F. Nie, A. Morton (Eds.) Pricm 7, Pts 1-3, 2010, pp. 2875-2878.

[10] N. Trofimenko, M. Kusnezoff, A. Michaelis, Recent Development of Electrolyte Supported Cells with High Power Density, in: S.C. Singhal, K. Eguchi (Eds.) Solid Oxide Fuel Cells 12, Electrochemical Society Inc, Pennington, 2011, pp. 315-325.

[11] D. Roehrens, U. Packbier, Q. Fang, L. Blum, D. Sebold, M. Bram, N. Menzler, Materials (Basel, Switzerland), 9 (2016) 762.

[12] N.P. Brandon, D. Corcoran, D. Cummins, A. Duckett, K. El-Khoury, D. Haigh, R. Leah, G. Lewis, N. Maynard, T. McColm, R. Trezona, A. Selcuk, M. Schmidt, Journal of Materials Engineering and Performance, 22 (2013) 2900-2903.

[13] M. Brandner, M. Bram, J. Froitzheim, H.P. Buchkremer, D. Stöver, Solid State Ionics, 179 (2008) 1501-1504.

[14] W.J. Quadakkers, J. Piron-Abellan, V. Shemet, L. Singheiser, Materials at High Temperatures, 20 (2003) 115-127.

[15] S. Harboe, A. Schreiber, N. Margaritis, L. Blum, O. Guillon, N.H. Menzler, (2019 - in review).

[16] D.J.L. Brett, A. Atkinson, N.P. Brandon, S.J. Skinner, Chem. Soc. Rev., 37 (2008) 1568-1578.

[17] M. Cassidy, S. Boulfrad, J. Irvine, C. Chung, M. Jorger, C. Munnings, S. Pyke, Fuel Cells, 9 (2009) 891-898.

[18] E. Matte, G. Holzlechner, L. Epple, D. Stolten, P. Lupetin, Journal of Power Sources, 413 (2019) 334-343.

[19] S. Ando, O. Okamoto, K. Hayama, S. Furuya, Y. Momiyama, N. Isaka, M. Sato, S. Tanaka, T. Hoshiko, N. Watanabe, Y. Kakinuma, in, 2014, pp. 23.

[20] M.N. I., D.O. V., M.J. V., S. G., AIChE Journal, 43 (1997) 2832-2836.

[21] F. Heilmann, G. Rixecker, F.D. Börner, W. Lippmann, A. Hurtado, Journal of the European Ceramic Society, 29 (2009) 2783-2789.

[22] H. Takei, T. Kobayashi, Journal of Crystal Growth, 23 (1974) 121-124.

[23] W. Jordan, J.J. Naughton, Am. Mineralogist, 48 (1963).

[24] K. Ando, H. Kurokawa, Y. Oishi, H. Takei, Journal of the American Ceramic Society, 64 (1981) C30-C30.

[25] U. Nurbaiti, Darminto, Triwikantoro, M. Zainuri, S. Pratapa, Ceramics International, 44 (2018) 5543-5549.

[26] F. Tavangarian, R. Emadi, Ceramics International, 37 (2011) 2275-2280.

[27] J.M. Burlitch, M.L. Beeman, B. Riley, D.L. Kohlstedt, Chemistry of Materials, 3 (1991) 692-698.

[28] R. Gheitanchi, M. Kharaziha, R. Emadi, Ceramics International, 43 (2017) 12018-12025.

[29] Y. Lai, X. Tang, X. Huang, H. Zhang, X. Liang, J. Li, H. Su, Journal of the European Ceramic Society, 38 (2018) 1508-1516.
[30] S.H. Tamin, N.A. Dzulkurnain, S. Adnan, M.H. Jaafar, N.S. Mohamed, Journal of Sol-Gel Science and Technology, 86 (2018) 24-33.
[31] E. Matte, P. Lupetin, D. Stolten, N.B. (Ed.), Proceedings of European Fuel Cell Forum, (2016).
[32] H. Yokokawa, H.Y. Tu, B. Iwanschitz, A. Mai, Journal of Power Sources, 182 (2008) 400-412.
[33] F. Tietz, Q. Fu, V.A.C. Haanappel, A. Mai, N.H. Menzler, S. Uhlenbruck, International Journal of Applied Ceramic Technology, 4 (2007) 436-445.
[34] S.P. Simner, M.D. Anderson, M.H. Engelhard, J.W. Stevenson, Electrochemical and Solid State Letters, 9 (2006) A478-A481.
[35] F. Han, R. Muecke, T. Van Gestel, A. Leonide, N.H. Menzler, H.P. Buchkremer, D. Stover, Journal of Power Sources, 218 (2012) 157-162.
[36] R. Shannon, Acta Crystallographica Section A, 32 (1976) 751-767.
[37] W. Lee, J.W. Han, Y. Chen, Z. Cai, B. Yildiz, Journal of the American Chemical Society, 135 (2013) 7909-7925.
[38] L. Kindermann, D. Das, D. Bahadur, R. Wei, H. Nickel, K. Hilpert, Journal of the American Ceramic Society, 80 (1997) 909-914.
[39] N.H. Menzler, P. Batfalsky, A. Beez, L. Blum, S. Groß-Barsnick, L. Niewolak, W. J. Quadakkers, R. Vaßen, in: 12th European SOFC & SOE Forum 2016, Lucerne/Switzerland, 2016, pp. 290-297.
[40] A. Ashour, M.A. Kaid, N.Z. El-Sayed, A.A. Ibrahim, Applied Surface Science, 252 (2006) 7844-7848.
[41] P.S. Patil, Materials Chemistry and Physics, 59 (1999) 185-198.
[42] J. Stevenson, T. Armstrong, R. Carneim, L. Pederson, W. Weber, Journal of the Electrochemical Society, 143 (1996) 2722-2729.
[43] R.H.E. van Doorn, H.J.M. Bouwmeester, A.J. Burggraaf, Solid State Ionics, 111 (1998) 263-272.
[44] I. Wærnhus, N. Sakai, H. Yokokawa, T. Grande, M.-A. Einarsrud, K. Wiik, Solid State Ionics, 175 (2004) 69-71.
[45] H.L. Lein, K. Wiik, T. Grande, Solid State Ionics, 177 (2006) 1587-1590.
[46] B. Wang, B. Zydorczak, Z.-T. Wu, K. Li, Journal of Membrane Science, 344 (2009) 101-106.
[47] H. Ding, A.V. Virkar, M. Liu, F. Liu, Physical Chemistry Chemical Physics, 15 (2013) 489-496.